

A Thesis Submitted for the Degree of PhD at the University of Warwick

Permanent WRAP URL:

<http://wrap.warwick.ac.uk/101927/>

Copyright and reuse:

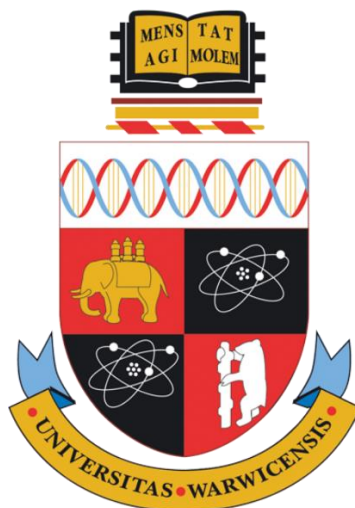
This thesis is made available online and is protected by original copyright.

Please scroll down to view the document itself.

Please refer to the repository record for this item for information to help you to cite it.

Our policy information is available from the repository home page.

For more information, please contact the WRAP Team at: wrap@warwick.ac.uk



Understanding the formation and responsive behavior of aqueous polymer self-assemblies

Lewis David Blackman

Submitted for the degree of Doctor of Philosophy

University of Warwick

Department of Chemistry

September 2017



For Charlotte Davison and Maria Blackman.

Table of Contents

Table of Contents	I
List of Figures, Schemes and Tables	IV
List of Figures	IV
List of Schemes	XVI
List of Tables	XVII
Acknowledgements	XVIII
Declaration of Authorship	XXI
Publications	XXIII
Abbreviations	XXVI
1. Introduction	1
1.1. Declaration of Authorship	2
1.2. Polymers and Synthetic Techniques.....	3
1.2.1. Introduction to polymers.....	3
1.2.2. Chain-growth polymerization and polymer architectures	5
1.2.3. Reversible deactivation radical polymerization (RDRP).....	8
1.2.4. RAFT polymerization	9
1.2.5. Photo-RAFT polymerization	15
1.3. Polymer Solution Self-Assembly	19
1.3.1. Polymer self-assembly under thermodynamic control.	19
1.3.2. Polymer self-assembly under kinetic control.....	24
1.4. Polymerization-Induced Self-Assembly.....	29
1.4.1. Polymerization-induced self-assembly <i>via</i> thermal initiation	32
1.4.2. Polymerization-induced self-assembly <i>via</i> photoinitiation.....	34
1.5. Stimuli-Responsive Polymers and Polymer Self-Assemblies.....	38
1.5.1. CO ₂ and pH-responsive polymer systems.	38
1.5.2. Light-responsive polymer systems	41
1.5.3. Polymer systems responsive to other stimuli.....	43
1.6. Analysis Techniques for Polymer Self-Assemblies	46
1.6.1. Light scattering techniques	46
1.6.2. Electron microscopy techniques	55
1.7. Summary	61
1.8. References	62
2. Effect of micellization on the thermoresponsive behavior of polymeric assemblies..	66

2.1. Declaration of Authorship	67
2.2. Abstract	68
2.3. Introduction	69
2.4. Results and Discussion	80
2.4.1. Polymer synthesis and micelle preparation	80
2.4.2. Critical micelle concentration (CMC) determination	83
2.4.3. Variable temperature light scattering analysis.....	86
2.4.4. Variable temperature turbidimetry and microcalorimetry analysis	88
2.4.5. Discussion of micelles with longer pNIPAM coronas	94
2.5. Conclusion.....	97
2.6. Experimental Section.....	98
2.6.1. Methods and materials	98
2.6.2. Polymer synthesis	99
2.6.3. Particle analysis	101
2.7. References	104
3. Probing the causes of thermal hysteresis using tunable N_{agg} micelles with linear and brush-like thermoresponsive coronas.....	107
3.1. Declaration of Authorship	108
3.2. Abstract	109
3.3. Introduction	110
3.4. Results and Discussion	117
3.4.1. Polymer synthesis and micelle preparation	117
3.4.2. Multiple angle light scattering analysis.	121
3.4.3. Thermoresponsive behavior.....	122
3.5. Conclusion.....	133
3.6. Experimental Section.....	134
3.6.1. Methods and materials	134
3.6.2. Synthetic procedures.....	136
3.7. References	150
4. Comparison of photo- and thermally initiated polymerization-induced self-assembly: a lack of end group fidelity drives the formation of higher order morphologies.....	153
4.1. Declaration of Authorship	154
4.2. Abstract	155
4.3. Introduction	156
4.4. Results and Discussion	160
4.4.1. Construction and Comparison of Isothermal Phase Diagrams	160
4.4.2. The influence of light intensity on the final PISA morphology	169

4.4.3. The influence of post-synthetic light and heat irradiation on the pre-formed PISA morphologies.....	172
4.4.4. Investigation into the equilibrium morphologies formed at 37 °C	179
4.5. Conclusion.....	182
4.6. Experimental Section.....	183
4.6.1. Methods and materials	183
4.6.2. Synthetic procedures.....	185
4.7. References	192
5. PISAylation: Confinement of functional and therapeutic proteins in selectively permeable polymersomes.....	194
5.1. Declaration of Authorship	195
5.2. Abstract	196
5.3. Introduction	197
5.4. Results and Discussion	206
5.4.1. Polymer synthesis	206
5.4.2. Preparation of GFP-loaded vesicles for direct fluorescence imaging.....	208
5.4.3. Preparation of catalytic HRP-loaded vesicles.....	211
5.4.4. Preparation of GOx-loaded vesicles and enzymatic cascade activity.....	214
5.4.5. Calculation of loading efficiency.....	218
5.4.6. Preparation of ASNS-loaded vesicles as an alternative to PEGylation	222
5.4.7. <i>In vitro</i> efficacy of ASNS-loaded vesicles towards a cancer cell line.....	228
5.5. Conclusion.....	232
5.6. Experimental Section.....	233
5.6.1. Methods and materials	233
5.6.2. Recombinant GFP expression and purification	236
5.6.3. Particle synthesis	238
5.6.4. Kinetic colorimetric analyses	239
5.6.5. Calculation of protein loadings.....	240
5.6.6. <i>In vitro</i> cell studies.....	241
5.7. References	243
6. Conclusions and Outlook	245
7. Appendix	250
7.1. Technical note	250
7.2. Supplementary SEC Data	252

List of Figures, Schemes and Tables

List of Figures

Figure 1.1. Examples of some common chain architectures. Colored spheres represent different monomers and gold stars or triangles represent different initiators or initiating groups.	7
Figure 1.2. Compatibility of the R- and Z-groups with different monomers. The groups are listed in order of decreasing of fragmentation rates (R-groups) or addition rates (Z-groups). A bold line shows good control over both molar mass and dispersity. A dashed line shows partial control or significant retardation. Abbreviations: MMA=methyl methacrylate, HPMAM=2-hydroxypropyl methacrylamide, St=styrene, MA=methyl acrylate, AM=acrylamide, AN=acrylonitrile, VAc=vinyl acetate, NVP=N-vinylpyrrolidone, NVC=N-vinylcarbazole. Adapted from ref. ¹⁵	12
Figure 1.3. Outline of the species obtained from a homopolymerization and single chain extension by a RAFT polymerization process at full monomer conversion. Taken from ref. ⁸	13
Figure 1.4. LHS: Chemical structures of some common photoinitiators and photocatalysts. RHS: The mechanism of PET-RAFT in the absence (oxidative quenching) and presence (reductive quenching) of a sacrificial electron donor, TEA. Adapted from ref. ¹⁸	16
Figure 1.5. Illustration of the effect of the packing parameter, p , on the equilibrium morphology based on geometric arguments for diblock copolymers. Taken from ref. ³²	20
Figure 1.6. Isothermal equilibrium phase diagram for PS- <i>b</i> -PAA nanostructures formed at various SDS concentration and water content at a polymer concentration of 1.0 wt%. The phase regions are separated by solid black lines, the dashed lines are a guide for the eye. Key: S = spheres, R = rods, V = vesicles. Adapted from ref. ³⁶	22
Figure 1.7. Illustration of the unimer exchange mechanism between “dynamic” particles to reach an equilibrium state in a given timeframe, and of the particle-particle fusion mechanism.	24
Figure 1.8. A: Non-equilibrium trapped structures and B: mixed and hybrid morphologies observed for various PS- <i>b</i> -PAA and poly(styrene)- <i>b</i> -poly(ethylene oxide) (PS- <i>b</i> -PEO) polymers. Adapted from ref. ⁴⁴	25
Figure 1.9. Formation of non-equilibrium non-spherical polymersome structures. A: Morphological transition from a spherical polymersome towards a stomatocyte during dialysis with representative cryo-TEM images. B: TEM images showing the transition from a lyotropic phase towards tubular polymersomes and finally spherical polymersomes with time during thin film rehydration. Adapted from ref. ⁴⁵ and ref. ⁴⁶ ..	27
Figure 1.10. A: Schematic of a typical PISA process by chain extension from one of the three different mCTA stabilizer blocks shown, to yield self-assembled amphiphilic diblock copolymer nano-objects in situ. B: Phase diagrams for an aqueous PGMA- <i>b</i> -PHPMA system using a long (top) or short (bottom) stabilizer block. Key: S = spheres, W = worms, BW = branched worms V = vesicles. Adapted from ref. ⁴⁷ and ref. ⁴⁸	29

Figure 1.11. Chemical structures of some corona-forming and core-forming blocks compatible with PISA in aqueous solution.	31
Figure 1.12. Functionalization of PISA-derived nano-objects formed by thermal initiation. A: Surface functionalization of PISA nano-objects with negative MRI contrast agents. B: Core functionalization of PISA nano-objects with fluorescent moieties. Adapted from ref. ⁶⁷	33
Figure 1.13. Structures of some typical PISA initiators and their corresponding initiator mechanisms. Key: TI = thermal initiator, PI = photoinitiator, PC = photocatalyst. Adapted from ref. ⁵³	35
Figure 1.14. Top: Mechanism for photoinitiation in the presence of dissolved oxygen using EY as the dye molecule and ascorbic acid as the reducing agent. Bottom: SEC traces and stained TEM images of some formed nano-objects under non-degassed conditions using ultra low volumes. Adapted from ref. ²⁴	37
Figure 1.15. Examples of some pH- and CO ₂ -responsive polymers outlined in the main text.....	39
Figure 1.17. Structures of some light-responsive polymers with photo-labile side chain moieties that undergo either reversible or irreversible phase transitions. In each case the aqueous solubility is indicated.	41
Figure 1.18. Structures of some multi-stimuli responsive polymers prepared by Thayumanavan and co-workers. Adapted from ref. ¹⁰⁴	43
Figure 1.19. A: Structure of the PEO-b-PAGMA hydrogen sulfide-responsive block copolymer used by Yan et al. and the H ₂ S-triggered cascade elimination reaction. B: Schematic of the self-assembly into polymersomes and disruption in the presence of H ₂ S. Taken from ref. ¹¹¹	44
Figure 1.20. Illustration of the relationship between the scattering wave vector and the incident and scattered wave vector. Taken from ref. ¹¹⁶	47
Figure 1.21. Illustration of how q affects the window of observation in a sample of polymer coils in solution. Larger q values probe a higher magnification (smaller features) of the sample. Taken from ref. ¹¹⁶	47
Figure 1.22. A: Example of an intensity autocorrelation function obtained from polymer 8 from Chapter 3 at an angle of 80°. B: The distribution of relaxation times obtained from fitting the autocorrelation function shown in A using the REPES algorithm.	49
Figure 1.23. Plot of τ^{-1} vs. q^2 for polymer 8 in Chapter 3 at a concentration of 1 mg·mL ⁻¹ to determine the apparent diffusion coefficient, D . The error bars represent 10% error.	50
Figure 1.24. Partial Zimm plot of polymer 8 at a concentration of 1 mg·mL ⁻¹ in Chapter 3. The reciprocal of the $M_{w, \text{particle}}$ is shown. The error bars represent 10% error.	53
Figure 1.25. Relationship between the intensity-weighted size distribution obtained from fitting the autocorrelation function of an equal mixture of two spheres of sizes one order of magnitude apart and the corresponding physical volume-weighted and number-weighted distributions. Taken from ref. ¹¹⁸	54
Figure 1.26. Dry state TEM images of PEG ₁₁₃ -HPMA ₃₀₀ formed by PISA at 10 wt% HPMA by thermal initiation from Chapter 4 on a Formvar-coated grid stained with 1% uranyl acetate solution. Image A shows a positively stained region. Image B shows a	

region with a greater coverage of the uranyl acetate stain, resulting in negative staining.	57
Figure 1.27. Cryo-TEM images of some common contaminants. A: Empty vitreous ice. B: Hexagonally packed ice. C: Large ice crystals (white arrow). D: Probable ethane contamination (white arrows). The scale bars represent 200 nm. Taken from ref. ¹²²	59
Figure 2.1. Hypothetical phase diagram for a polymer system in solution that exhibits both LCST and UCST behavior. Blue chains represent solvated chains and red, collapsed chains represent solvophobic, collapsed chains that precipitate and macroscopically phase separate from the surrounding solvent. The coexistence (solid lines) and spinodal (dashed lines) curves are shown. ϕ = composition.....	69
Figure 2.2. Chemical structures of some typical homopolymers derived from vinylic monomers that exhibit either LCST or UCST-type behavior. ¹	70
Figure 2.3. Left: Post-polymerization route to thermoresponsive homo-, co- and terpolymers from a common pVDMA precursor polymer scaffold. Abbreviations of the monomers shown in blue, green and red are shown along with their role on the overall phase behavior. Right: Turbidimetry data showing UCST (A), LCST (B) and both LCST and UCST (C) behavior. Arrows indicate the solubility of the polymer at a given point along the turbidimetry curve. Adapted from ref. ⁴¹	71
Figure 2.4. End group modification of thermoresponsive polymers to produce dual-responsive polymers. A: Chemical structure of catechol-functionalized pNIPAM (top) and soluble-to-insoluble transition induced by either increasing the temperature or the addition of Fe^{3+} (bottom). Adapted from ref. ⁴⁴ B: Chemical structure of azobenzene-functionalized pOEGMA (top) and illustration of how the soluble-to-insoluble transition induced by increasing the temperature could be reversed by either cooling, or 365 nm light irradiation to undergo the trans-to-cis isomerization of the end group (bottom). Adapted from ref. ⁴⁵	73
Figure 2.5. Triple fluorescent overlaid confocal microscopy images of fluorescently labelled p(NIPAM-co-DMA)-b-pLA) micelles (green channel) incubated with bovine epithelial cells with selectively stained nuclei (blue channel) and either lysosomes (A and B, red channel) or golgi apparatus and ER (C and D, red channel). Incubation at 37 °C (A and C) and 42 °C (B and D) are shown. Areas where green and red overlap are indicated in yellow. Taken from ref. ²¹	75
Figure 2.6. Turbidimetry analysis showing the thermal transition of pNIPAM in aqueous solution. The polymer's solubility in different temperature regimes is shown, along with the hysteresis. Adapted from ref. ⁴⁹	76
Figure 2.7. Left: Chemical structure of doubly pH-responsive p(DMAEMA-co-DEAEMA)-b-DMAEMA used in the study by O'Reilly and co-workers. Right: Increasing N_{agg} with decreasing α for a series of block copolymers with increasing DEAEMA incorporation, denoted here as 1-4. Adapted from ref. ⁶²	79
Figure 2.8. ^1H NMR spectrum of mCTA1 , analyzed at 400 MHz in CDCl_3	81
Figure 2.9. SEC RI chromatograms of mCTA1 using 5 mM NH_4BF_4 in DMF as the eluent and calibrated against poly(methyl methacrylate) standards.	81
Figure 2.10. SEC RI chromatograms of mCTA1 and polymer 1 using 5 mM NH_4BF_4 in DMF as the eluent and calibrated against PMMA standards.....	82
Figure 2.11. ^1H NMR spectrum of polymer 1 , analyzed at 400 MHz in CDCl_3	83

Figure 2.12. Fluorescence emission spectra of polymer **2** at 0.2 μM PNA dye concentration at varying polymer concentrations. The excitation wavelength was 340 nm. I_{micelle} and I_{water} are shown with dashed arrows illustrating the decrease or increase in intensity with decreasing polymer concentration..... 84

Figure 2.13. Plot of $I_{\text{micelle}}/I_{\text{water}}$ against $\log[\text{polymer}]$ for micelles comprised of polymer **1** (black squares), **2** (red circles), **3** (blue triangles), **4** (pink triangles) and **5** (green diamonds) using 0.2 μM PNA dye. The data in each series was normalized to the maximum intensity of the highest polymer concentration in that series..... 85

Figure 2.14. Multiple-angle light scattering analysis of micelles **1-5** in water. **A.** Autocorrelation function of polymer **2** at 20 $^{\circ}\text{C}$ analyzed at an angle of 150 $^{\circ}$. The inset shows the y-axis as a log scale. **B.** Plot of the τ^{-1} values obtained by DLS analysis against q^2 for polymer **2** at 20 $^{\circ}\text{C}$ with 10 % error bars. **C.** Partial Zimm plot of polymer **2** at 20 $^{\circ}\text{C}$ with 10% error bars obtained using SLS analysis. **D.** Plot of N_{agg} with varying nBA units in the micellar core determined by SLS analysis for the micellar series **1-5** at 20 $^{\circ}\text{C}$ with 10% error bars..... 86

Figure 2.15. Left: Variation of R_{H} of micelles composed of polymers **1** (black squares), **2** (red circles), **3** (blue triangles) and **4** (pink triangles) with temperature as determined by DLS analysis. Inset: Variation of R_{H} (filled circles) and R_{g} (empty circles) of a pNIPAM-stabilized dendritic core particle as determined by DLS and SLS, taken from ref.⁶⁹ Two clear transitions were observed in the referenced work. Right: Variation of R_{core} of micelles composed of polymers **1** (black squares), **2** (red circles), **3** (blue triangles) and **4** (pink triangles) with temperature as determined by SLS analysis. Error bars represent 10% error in R_{core} 88

Figure 2.16. Thermal analysis of micelles comprised of polymer **1**. Heating traces from the turbidimetry (A) and microcalorimetry (B) analysis are shown along with the cloud point from turbidimetry and T_{p} from microcalorimetry. The inset images show digital photographs of the micelles before and after heating above the transition temperature. Both were performed at 1 $\text{mg}\cdot\text{mL}^{-1}$ with a temperature ramp of 1 $^{\circ}\text{C}\cdot\text{min}^{-1}$ 89

Figure 2.17. A: Temperature of phase transitions measured by variable temperature techniques at 1 $\text{mg}\cdot\text{mL}^{-1}$ with 10% error bars. Black squares represent cloud points determined by turbidimetry. Red circles represent T_{p} values determined by microcalorimetry. B: Degree of hysteresis observed by turbidimetry analysis. Error bars represent the standard deviation over 3 repeats. C: Heating (solid) and cooling (dashed) turbidimetry traces at 1 $\text{mg}\cdot\text{mL}^{-1}$ for micelles comprised of polymer **1** D: Heating (solid) and cooling (dashed) turbidimetry traces at 1 $\text{mg}\cdot\text{mL}^{-1}$ for micelles comprised of polymer **5**. In all experiments, the heating and cooling rate was 1 $^{\circ}\text{C}\cdot\text{min}^{-1}$ 90

Figure 2.18. A. Turbidity of micelles comprised of polymer **5** with time at 30 $^{\circ}\text{C}$ after being heated to 40 $^{\circ}\text{C}$. Error bars represent the standard deviation over 3 repeats. B. Schematic representation of higher chain density in high N_{agg} micelles leading to higher interchain entanglement in the globular state, above the transition temperature. C. Schematic representation of increased water exclusion in highly hydrophobic micelles above the transition temperature, compared to less hydrophobic cores, which exhibit more hydrated precipitates. 91

Figure 2.19. Plot of η_0 against polymer concentration. η_0 values were calculated from the obtained absolute viscosity values, η , and the measured viscosity of the pure solvent, η_{s} ,

using $\eta_0 = (\eta - \eta_s) / \eta_s$. Error bars represent the standard deviation across the shear rates. In each case the error bars are smaller than the data point marker.	93
Figure 2.20. A. Triple detection SEC of mCTA1a using 5 mM NH_4BF_4 in DMF as the eluent. B. SEC RI traces of mCTA1a (solid line) and polymer 5a (dashed line) using 2% triethylamine in chloroform as the eluent and calibrated against poly(styrene) standards. C. Quantitative ^{13}C NMR spectrum of polymer 5a with the integrals set relative to carbon environment e.	95
Figure 2.21. Turbidimetry analysis of mCTA1a (A) and polymers 5a (B) and 5 (C) at 1 mg mL ⁻¹ . In each case the heating (solid lines) and cooling traces (dashed lines) are shown and the polymer composition has been included for comparison.	96
Figure 2.22. ^1H NMR spectra of micelles comprised of polymer 4 (top) and polymer 1 (bottom) obtained at 500 MHz in D_2O . Proton signals from the side chains have been indicated in each case.	96
Figure 3.1. Chemical structures of various LCST-type polymers discussed, which show poor reversibility. pMPA, a polymer that shows good reversibility, has been included for comparison purposes.	113
Figure 3.2. Illustration of the thermoresponsive diblock copolymers used in this study. Key: x = mol% nBA in the core-forming block. Below is a table outlining the differences in the corona blocks' properties.	115
Figure 3.3. A: Schematic of one series of diblock copolymers with identical corona-forming blocks and tunable p(nBA-co-DMA) core compositions that self-assemble in water to yield micelles with a tunable N_{agg} . The resulting particles show identical cloud points but different thermal hysteresis when heated in solution. B: Design of four micellar series with different corona-forming blocks with distinct chemistry and architecture, but whose cores contain the same p(nBA-co-DMA) compositions. In each case, the chemical structure of the corona block is shown. C: Studying the thermoresponsive behaviors of the four micellar series gives information on the structure-property relationships regarding thermal hysteresis in thermoresponsive self-assemblies.	116
Figure 3.4. SEC RI chromatograms of diblock copolymers with pNIPAM coronas (A), pDEAm coronas (B), pDEGMA coronas (C) and pOEGMA coronas (D) alongside their corresponding mCTAs. For mCTA1 and polymer 1 (panel A), 5 mM NH_4BF_4 in DMF was used as the eluent. For all other experiments, 2% TEA in THF was used as the eluent. In each case, the distributions were calculated using the RI traces calibrated against poly(methyl methacrylate) standards.	119
Figure 3.5. ^1H NMR spectra of mCTA2 (top) and polymer 8 (middle). The bottom spectrum is that of mCTA2 subtracted from that of polymer 8 used to calculate the core composition; the peaks at 4.00 and 3.22 - 2.77 ppm corresponding to pnBA and pDMA, respectively, are clearly resolved.	120
Figure 3.6. Representative multiple angle dynamic (above) and static (below) light scattering data of micelles comprised of polymers 10 (A), 15 (B) and 17 (C), each at 1 mg·mL ⁻¹ . Error bars represent 10% error.	121
Figure 3.7. Variation in the particles' N_{agg} with the molar fraction of hydrophobic nBA in the core-forming block, as determined by SLS analysis. Micelles with pNIPAM (polymers 1-5 , blue triangles), pDEAm (polymers 6-10 , orange circles), pDEGMA	

(polymers 11-15 , purple squares) and pOEGMA coronas (polymers 16-17 , cyan squares) are shown. Error bars represent 10% error.....	122
Figure 3.8. A: Variation of the cloud point transition temperatures of polymers 1-5 (orange circles), 6-10 (blue triangles) and 11-15 (purple squares) with the molar fraction of hydrophobic nBA in the core-forming block, as determined by turbidimetry. Error bars represent 10% error. B: Variation of thermal hysteresis of micelles comprised of pDEAm coronas, which cannot form hydrogen bonds between polymer chains (polymers 1-5 , orange bars), and pNIPAM coronas, which can (polymers 6-10 , blue bars). Values determined by turbidimetry and plotted as a function of mol% nBA in the core-forming block. Error bars represent the standard deviation across 3 repeats.	123
Figure 3.9. Variable temperature turbidimetry analysis of micelles comprised of polymers 1 (A), 5 (B), 6 (C) and 10 (D) at 1 mg·mL ⁻¹ with a heating and cooling rate of 1 °C·min ⁻¹ . In each case, the solid trace represents the heating cycle and the dashed trace represents the cooling cycle.	124
Figure 3.10. Turbidimetry analyses of micelles with pDEGMA coronas. Turbidimetry curves for polymers 11 (red) and 15 (black) are shown. In each case, solid lines represent heating cycles and dashed lines represent cooling cycles. The insets show photographs of solutions before heating (A) and after heating followed by storage at 4 °C for 13 months (B).	127
Figure 3.11. Chain density of micelles comprised of polymers 11-15 . Error bars represent 10% error. The two distinct regimes of reversible and irreversible phase transitions are marked with dashed lines. Note that polymer 14 (88% nBA in the core forming block) shows the highest chain density because its R _H is smaller than that of polymer 15 (100% nBA in the core forming block).	128
Figure 3.12. Turbidimetry analyses of micelles with pOEGMA coronas. Turbidimetry curves for polymers 16 (red) and 17 (black) are shown. In each case, solid lines represent heating cycles and dashed lines represent cooling cycles. For clarity, some instances of macroscopic precipitation and sedimentation have been labelled and the cooling curve for polymer 17 has been smoothed.	129
Figure 3.13. A: SEC RI chromatograms of polymer 17 before (black dashed line) and after (red solid line) three heating and cooling cycles from 50 - 95 °C. 2% TEA in THF was used as the eluent and the instrument was calibrated against PMMA standards. In each case, the distributions were calculated using the RI traces. B: Variable temperature turbidimetry analysis of micelles comprised of polymer 17 at 1 mg·mL ⁻¹ heated from 50 - 70 °C so as to reduce the thermal annealing time. In each case, the solid trace represents the heating cycle and the dashed trace represents the cooling cycle. The 1 st cycle (black traces), 2 nd cycle (red traces) and 3 rd cycle (blue traces) are shown.	130
Figure 3.14. ¹ H (top) and ¹³ C DEPT (bottom) NMR spectra of DEAm, analyzed at 400 and 100 MHz respectively, in CDCl ₃	137
Figure 3.15. ¹ H (top) and ¹³ C DEPT (bottom) NMR spectra of 2-Cyano-2-propyl dodecyl trithiocarbonate analyzed at 400 and 100 MHz respectively, in CDCl ₃	140
Figure 3.16. ¹ H (above) and ¹³ C DEPT (below) NMR spectra of 4-cyano-4-(((ethylthio)carbonothioyl)thio) pentanoic acid, analyzed at 400 and 100 MHz respectively, in CDCl ₃	142

Figure 3.17. ^1H (above) and ^{13}C DEPT (below) NMR spectra of methyl 4-cyano-4-(((ethylthio) carbonothioyl)thio) pentanoate, analyzed at 300 and 75 MHz respectively, in CDCl_3 .	144
Figure 3.18. ^1H NMR spectrum of mCTA2 , analyzed at 400 MHz in CDCl_3 .	145
Figure 3.19. ^1H NMR spectrum of mCTA3 , analyzed at 400 MHz in CDCl_3 .	146
Figure 3.20. ^1H NMR spectrum of mCTA4 , analyzed at 400 MHz in CDCl_3 .	147
Figure 4.1. Chemical structure and representative ^1H NMR spectra of $\text{PEG}_{113}\text{-b-PHPMA}_x$ diblock copolymers formed at 10 wt% HPMA by route B analyzed at 300 MHz in CD_3OD . The spectral intensities were normalized to the PEG mCTA at 3.63 ppm (signal “b”) and their baselines off-set for clarity.	160
Figure 4.2. Representative RI SEC traces for $\text{PEG}_{113}\text{-b-PHPMA}_x$ diblock copolymers formed at 10 wt% HPMA using 5 mM NH_4BF_4 in DMF as the eluent. Data for route A (I) and route B (II) are shown along with the \bar{D} values. Key: In each case, PEG_{113} (black trace), $\text{PEG}_{113}\text{-b-PHPMA}_{100}$ (red trace), $\text{PEG}_{113}\text{-b-PHPMA}_{200}$ (green trace), $\text{PEG}_{113}\text{-b-PHPMA}_{300}$ (magenta trace) and $\text{PEG}_{113}\text{-b-PHPMA}_{400}$ (blue trace) are shown. Panel III shows the calculated M_n values for route A (red circles) and route B (black squares) derived diblock copolymers shown in panels I and II, using PMMA standards. Error bars represent 10% error. The black linear trend shows the theoretical M_n values. Panel IV shows SEC data from the kinetic study of $\text{PEG}_{113}\text{-b-PHPMA}_{300}$ formed by routes A (red) and B (black). Left axis: M_n values of polymers formed by route A (red circles) and route B (black squares), the black linear trend shows the theoretical M_n values. Right axis: \bar{D} values of polymers formed by route A (red diamonds) and route B (black diamonds).	162
Figure 4.3. UV-Vis spectrum of PP-OH (black) with the wavelength range of the light source indicated with a purple box. Below are examples of $\text{PEG}_{113}\text{-b-PHPMA}_{400}$ formulations at 10 wt% formed by route A either in the presence or absence of the photoinitiator.	162
Figure 4.4. Kinetic plots of formulations formed by routes A (red circles) and B (black squares). In each case an inflection point has been indicated by the intercept of the two gradients, which shows the onset of particle aggregation.	163
Figure 4.5. Phase diagrams of PISA formulations synthesized by routes A (I) and B (II) with accompanying stained TEM images. Scale bars represent 0.5 μm , except where marked with an asterisk, in which case the scale bar represents 0.2 μm . Key: S = spheres, W = worms, L = lamellae, ULV = unilamellar vesicles, MLV = multilamellar vesicles. Formulations highlighted with red boxes will be discussed further in this section.	164
Figure 4.6. Photograph of $\text{PEG}_{113}\text{-b-PHPMA}_{100}$ formulations formed by thermally initiated PISA (route B). From left to right: 10 wt% HPMA, 15 wt% HPMA, 20 wt% HPMA and 25 wt% HPMA.	165
Figure 4.8. Stained TEM images of the $\text{PEG}_{113}\text{-b-PHPMA}_x$ copolymers, where x is denoted in each image, formed by thermally initiated PISA at 10 wt% HPMA. The scale bars represent 500 nm.	166
Figure 4.9. Histograms of $\text{PEG}_{113}\text{-b-PHPMA}_{400}$ diblock copolymer unilamellar vesicles formed at [HPMA] = 10 wt% by route A (green) and route B (red) measured from particle counting measurements on TEM images. In each case at least 200 particles were analyzed.	168

Figure 4.10. A: Kinetic study of the PEG₁₁₃-b-PHPMA₃₀₀ formulation at 10 wt% formed by route C (blue triangles) overlaid with the kinetic data previously obtained for that formed by route B (black squares). B: SEC data for the kinetic studies. Left axis: M_n values of polymers formed by route C (blue triangles) and route B (black squares), the black linear trend shows the theoretical M_n values. Right axis: \bar{D} values of polymers formed by route C (blue triangles) and route B (black diamonds). 169

Figure 4.11. Representative TEM images showing no morphology change in formulations formed by route C (photoinitiation 20% light intensity at 37 °C) post-synthetically treated with route F (irradiation with 20% light intensity at 37 °C for 18 h). PEG₁₁₃-b-PHPMA₃₀₀ at 10 wt% HPMA (top) and PEG₁₁₃-b-PHPMA₂₀₀ at 15 wt% HPMA (bottom) are shown. Scale bar = 500 nm. 170

Figure 4.12. Stained TEM images of particles from various formulations formed from route C (bottom row), shown in comparison to identical formulations formed from routes A (top row) and B (middle row). The scale bars each represent 500 nm. 171

Figure 4.13. Post-synthetic heat and light irradiation experiments. Stained TEM images of PEG₁₁₃-b-PHPMA₃₀₀ formulations obtained at [HPMA] = 10 wt% by route A (I) or route B (II), treated by route D (LHS) or route E (RHS). The scale bars represent 500 nm. III: DLS analysis (top) and photographs (bottom) of formulations formed by route A and routes A+D. Key: Route A – photoinitiated PISA at 100% light intensity at 37 °C. Route B – thermal initiation at 37 °C. Route D – photoirradiation at 100% light intensity at 37 °C for 18 h. Route E – incubation at 37 °C for 18 h. 173

Figure 4.14. SEC traces of PEG₁₁₃-b-PHPMA₃₀₀ at [HPMA] = 10 wt% formed by various synthetic and post-synthetic routes. I: Normalized RI traces of formulations formed by routes A, A+D and A+E. II: Normalized 309 nm traces of formulations formed by routes A, B and A+D. III: Normalized 309 nm traces of formulations formed by routes A and A+E. IV: Normalized 309 nm traces of formulations formed by routes C and C+F. Routes C and C+F are analogous experiments to A and A+D but at the lower light intensity irradiation. In each of the UV traces shown in II, III and IV the traces were normalized relative to the formulation formed by route B. The end group fidelity relative to route B is shown, along with the observed morphology determined by TEM. 175

Figure 4.15. Normalized SEC UV traces of PEG₁₁₃-b-PHPMA₄₀₀ formed at 10 wt% HPMA by route A (black) compared with those further irradiated with 100% light intensity for 18 h at 37 °C (route A+D) either with (green) or without (red) degassing the solution prior to irradiation. 176

Figure 4.16. MALDI-ToF MS analysis of PHPMA oligomers before (black) and after (blue) irradiation with heat and light at 100% light intensity for 18 h. 177

Figure 4.18. Representative stained TEM images showing morphology change of PEG₁₁₃-b-PHPMA₃₀₀ at 20 wt% obtained by route A and route A+D. Key: Route A = 100% light intensity photoinitiation at 37 °C. Route D = 100% light intensity photoirradiation at 37 °C for 18 h. 178

Figure 4.17. ¹H NMR spectroscopic analysis of PHPMA oligomers at 400 MHz in acetone-d₆ before (bottom) and after (top) irradiation with heat and light at 100% light intensity for 18 h. Removal of the ethylene protons adjacent to the trithiocarbonate end group at 3.31 ppm after irradiation has been highlighted. 178

Figure 4.19. Stained TEM images of equilibrium structures of diblock copolymers formed at 37 °C and 1 mg·mL ⁻¹ . The block ratio for each sample is indicated above the corresponding TEM image. The unlabeled scale bars = 200 nm.	179
Figure 4.20. Representative TEM images of the new equilibrium structure at 1 mg·mL ⁻¹ of PEG ₁₁₃ - <i>b</i> -PHPMA ₃₀₀ obtained by route A+D at 10 wt%.	180
Figure 4.21. ¹ H NMR spectrum of the PEG ₁₁₃ mCTA, analyzed at 300 MHz in CDCl ₃	186
Figure 4.22. ¹ H NMR spectrum of PHPMA oligomers analyzed at 300 MHz in (CD ₃) ₂ CO.	191
Figure 5.1. Various features of biomimetic self-assemblies. A: A multi-compartmentalized polymersome-in-polymersome system consisting of enzyme-loaded PS- <i>b</i> -PIAT polymersomes encapsulated within a larger PB- <i>b</i> -PEO polymersome. Taken from ref. ⁶ B: Time-resolved confocal microscopic analysis showing glycosylated giant polymersomes (red) binding with a cluster of ConA-functional PS beads (green). Taken from ref. ⁵ C: Enzyme-loaded PEO- <i>b</i> -PS stomatocytes catalyze the production of gases to achieve directional autonomous propulsion. Taken from ref. ⁷ D: Fatty acid liposomes allow the transport of external activated nucleotides into the lumen, which in turn results in template copying. Addition of externally applied amphiphiles results in insertion into the membrane and subsequent formation of daughter protocells. Taken from ref. ⁸	198
Figure 5.2. Outline of some methods for achieving polymersome permeability found in the literature. A: PS- <i>b</i> -PIAT polymersomes with intrinsic permeability towards small molecules. Taken from ref. ¹⁰ B: Post-synthetic chemical modification of PMOXA- <i>b</i> -PDMS- <i>b</i> -PMOXA vesicle membranes using a photoinitiator. Taken from ref. ¹¹ C: Incorporation of OmpF into PMOXA- <i>b</i> -PDMS- <i>b</i> -PMOXA vesicles to afford size-selective permeability. Adapted from ref. ¹² D: PNIPAM- <i>b</i> -PNBOCA vesicles show an irreversible enhancement in permeability in response to UV light irradiation. Adapted from ref. ¹³	199
Figure 5.3. Illustration of the artificial peroxisomes developed by Palivan and co-workers. A: A cell with its organelles. B: A natural peroxisome is a spherical liposome containing enzymes to break down ROS. C: Structure of the artificial peroxisome with enzymes in the lumen and OmpF in the membrane. D: Schematic of the enzymatic cascade reaction facilitated by the artificial peroxisomes. Taken from ref. ²⁰	201
Figure 5.4. SEC RI traces of the PEG ₁₁₃ mCTA (gray dashed line) and the PEG ₁₁₃ - <i>b</i> -PHPMA ₄₀₀ diblock copolymers (solid lines) comprising the protein-loaded vesicles used in this study. Empty vesicles (black trace), GFP-loaded vesicles (green trace), ASNS-loaded vesicles (purple trace), HRP-loaded vesicles (red trace) and GOx-loaded vesicles (blue trace) are shown, along with their calculated M _n and Đ values. 5 mM NH ₄ BF ₄ in N,N-dimethylformamide was used as the eluent and molecular weight distributions were calculated from poly(methyl methacrylate) standards.	206
Figure 5.5. Characterization of the empty vesicles. Column A: Representative dry state TEM images. The samples were stained with a 1 wt% uranyl acetate stain. Column B: Representative cryo-TEM image of empty vesicles in pH 5.5 phosphate buffer (top) and distribution of membrane thicknesses measured from statistical analysis (bottom). The error shows the standard deviation from 200 particle membranes. Column C: DLS analysis of empty vesicles in pH 5.5 phosphate buffer. The z-average hydrodynamic	

diameter (D_H) and polydispersity (PD) are shown. The error represents the standard deviation from 5 repeat measurements.	207
Figure 5.6. Characterization of GFP-loaded vesicles after purification. DLS autocorrelation function (A) and distribution (B) of GFP-loaded vesicles in pH 5.5 phosphate buffer. The D_H and PD are shown. The error represents the standard deviation from 5 repeat measurements. Representative dry state TEM images of samples stained with 1 wt% uranyl acetate (C and D). Representative cryo-TEM image of GFP-loaded vesicles in pH 5.5 phosphate buffer (E) and distribution of membrane thicknesses measured from statistical analysis (F). The error shows the standard deviation from 200 particle membranes.	209
Figure 5.7. A: Fluorescence spectra of the 1 st supernatant (red traces) and an identical concentration of the untreated protein (black traces). Insert: Photograph of the crude GFP-loaded vesicle solution immediately after the PISA reaction under a UV lamp. B: Fluorescence spectra of the 1 st supernatant (black traces), disassembled vesicle solution (red traces) and 2 nd supernatant (gray traces) in a 5:1 methanol:water solvent mixture. In each case the excitation spectra ($\lambda_{Em} = 512$ nm, dashed traces) and the emission spectra ($\lambda_{Ex} = 495$ nm, solid traces) are shown.	210
Figure 5.8. Fluorescence micrographs of free GFP (A), empty vesicles (B), empty vesicles purified from an identical GFP solution after light irradiation (C) and GFP-loaded vesicles (D). The scale bars represent 5 μ m.	211
Figure 5.9. Characterization of HRP-loaded vesicles after centrifugation/resuspension and preparative SEC. Column A: Representative dry state TEM images of samples stained with 1 wt% uranyl acetate. Column B: Representative cryo-TEM image of HRP-loaded vesicles in pH 5.5 phosphate buffer (top) and distribution of membrane thicknesses measured from statistical analysis (bottom). The error shows the standard deviation from 200 particle membranes. Column C: DLS analysis of HRP-loaded vesicles in pH 5.5 phosphate buffer. The D_H and PD are shown. The error represents the standard deviation from 5 repeat measurements.	212
Figure 5.10. Enzymatic activity of HRP-loaded vesicles. A: Schematic showing the HRP-catalyzed oxidation of DMB to its colored dimer product detected in the colorimetric assay. B: Activity of the HRP-loaded vesicles, empty vesicles and the empty vesicles purified from an identical HRP solution after 70 min light irradiation, measured by a change in absorbance at 492 nm. Reaction conditions: [Vesicles] = 3.3 mg·mL ⁻¹ , [H ₂ O ₂] = 3.5 % w/w, [DMB] = 0.4 mM in 80 mM pH 5.5 phosphate buffer. The error represents the standard deviation from 4 repeats.	213
Figure 5.11. Normalized preparative SEC RI traces of HRP-loaded vesicles (black trace) and that of the free HRP enzyme (red trace) in 100 mM pH 5.5 phosphate buffer. In each case, the injection volume was 1 mL.	214
Figure 5.12. Characterization of GOx-loaded vesicles after centrifugation/resuspension and preparative SEC. A and B: DLS analysis of GOx-loaded vesicles in pH 5.5 phosphate buffer. The D_H and PD are shown. The error represents the standard deviation from 5 repeat measurements. C and D: Representative dry state TEM images of samples stained with 1 wt% uranyl acetate. E and F: Representative cryo-TEM image of commercial GOx-loaded vesicles in pH 5.5 phosphate buffer and distribution of membrane thicknesses measured from statistical analysis (bottom). G and H: Representative cryo-	

TEM image in pH 5.5 phosphate buffer of vesicles loaded with GOx previously purified by dialysis, and distribution of membrane thicknesses measured from statistical analysis. In each case, the error shows the standard deviation from 200 particle membranes....215

Figure 5.13. Enzymatic activity of GOx-loaded vesicles. A: Schematic showing the GOx-catalyzed oxidation of D-glucose to δ -glucono-1,5-lactone and hydrogen peroxide. Excess HRP in solution was then used to catalyze the oxidation of DMB using the rate-limiting reagent hydrogen peroxide product from the first step. B: Activity of the GOx-loaded vesicles, empty vesicles, and empty vesicles purified from GOx after 70 min light irradiation (empty circles), measured by a change in absorbance at 492 nm. Reaction conditions: [Vesicles] = 3.3 mg·mL⁻¹, [D-glucose] = 17 mM, [free HRP] = 20 U·mL⁻¹, [DMB] = 0.4 mM in 70 mM pH 5.5 phosphate buffer. The error represents the standard deviation from 4 repeats.....216

Figure 5.14. Enzymatic activity of the HRP- and GOx-loaded vesicle cascade reaction. A: Schematic showing the HRP- and GOx-loaded vesicle cascade reaction using D-glucose as an initiating species resulting in production of the colored dimer after two steps. B: Activity of the HRP- and GOx-loaded vesicle cascade with all components present (orange circles), measured as an increase in absorbance at 492 nm. Negative control experiments with GOx-loaded vesicles alone (blue circles), HRP-loaded vesicles alone (red circles), or both vesicles with DMB but without D-glucose (gray circles) show no activity. Insets show end point photographs of the plate wells after 1.5 h. Reaction conditions (when all components present): [HRP vesicles] = 1.9 mg·mL⁻¹, [GOx vesicles] = 1.9 mg·mL⁻¹, [D-glucose] = 17 mM, [DMB] = 0.4 mM in 80 mM pH 5.5 phosphate buffer. The error represents the standard deviation from 4 repeats.217

Figure 5.15. Example data from BCA (A) and HPLC (B) analysis of the destroyed vesicles. A: A dilution series of known HRP concentrations in 5% SDS/ pH 5.5 phosphate buffer (black squares) was compared to the destroyed vesicles in 5% SDS/ pH 5.5 phosphate buffer (red circle). The data was not blank corrected. B: HPLC analysis of HRP at known concentrations.....218

Figure 5.16. Western blot analysis of disassembled GOx-loaded vesicles. A: Image of the developed blot. B: Obtained calibration curve of the dilution series.219

Figure 5.17. Comparison of the enzyme-loaded vesicles to the free enzymes. Activity data for HRP (A), GOx (B) and the HRP and GOx cascade (C) are shown. Panel D shows the residual activities calculated by comparing the slopes. The error bars represent the standard deviation from 4 repeats.221

Figure 5.18. Characterization of ASNS-loaded vesicles after purification. Column A: Representative dry state TEM images of samples stained with 1 wt% uranyl acetate. Column B: Representative cryo-TEM image of ASNS-loaded vesicles in pH 5.5 phosphate buffer (top) and distribution of membrane thicknesses measured from statistical analysis (bottom). The error shows the standard deviation from 200 particle membranes. Column C: DLS analysis of ASNS-loaded vesicles in pH 5.5 phosphate buffer. The D_H and PD are shown. The error represents the standard deviation from 5 repeat measurements.223

Figure 5.19. Schematic of the biosynthesis and uptake of L-asparagine. A: Healthy cells expressing L-asparagine synthetase are able to uptake L-asparagine from the external serum or synthesize their own from L-aspartate and L-glutamine. In the presence of L-

asparaginase, the supply of L-asparagine to healthy cells is achieved through biosynthesis inside the cell. B: Leukemia cells with low L-asparagine synthetase expression levels predominantly rely on circulating L-asparagine in the blood serum. In the presence of external L-asparaginase, the supply of L-asparagine to these cells is limited, thereby resulting in decreased proliferation. 224

Figure 5.20. A: Activity of the ASNS-loaded vesicles. The error bars represent the standard deviation across 4 repeats. B: Photographs of the end point wells of the first 6 supernatants, the empty vesicles purified from an ASNS solution after 70 min light irradiation, and the ASNS-loaded vesicles. C: Comparison of the free enzyme activity against the encapsulated enzyme. D: Comparison of the untreated ASNS activity to that of the first supernatant. Reaction conditions for vesicle solutions and free enzymes: [analyte mixture] = 85% v/v, [Nessler's reagent] = 15% v/v. Reaction conditions for discarded supernatants shown in panel B: [analyte mixture] = 10% v/v, [Nessler's reagent] = 15% v/v in deionized water. See experimental section for more details. 225

Figure 5.21. Proteolytic stability of ASNS-loaded vesicles. A: Activity of the α -CT-treated species (patterned bars) normalized to the activity of the untreated species (solid bars) after 18 h incubation for the ASNS-loaded vesicles, free ASNS and the PEGylated conjugate. B: Normalized activity after a 7 day incubation period. The error bars represent the standard deviation from 4 repeated measurements. C: Dry state TEM image of the ASNS-loaded vesicles after 7 days incubation with α -CT. The sample was stained with 1 wt% uranyl acetate. 226

Figure 5.22. Stability of the ASNS-loaded vesicles in human blood plasma. A and B: DLS size distribution and autocorrelation function after 4 days in blood plasma. The z-average D_H and PD are shown, with the error representing the standard deviation from 5 repeated measurements. Key: Intensity = red, volume = green, number = black. C: Stained TEM image of the ASNS-loaded vesicles after 4 days in blood plasma. 227

Figure 5.23. Preparation of gene silenced A549 cells as a model for lymphoblastic leukemia cells. A: Western blot analysis of lysed cultures of A549 cells, either untreated or treated with various siRNA (top). The pixel densitometry plots (bottom) are shown along with their average peak intensities. The error represents the standard deviation across 3 repeat (A549) or 2 repeat (siRNA groups) measurements. B: Proliferation in normal medium for A549 cells incubated with various siRNA. The error represents the standard deviation across at least 3 repeat experiments (control A549 cells, $n = 6$). Key: * $p \leq 0.05$, ** $p \leq 0.01$ 228

Figure 5.24. Schematic of the cell proliferation assay employed. After incubating the growth medium with either ASNS-loaded vesicles or empty vesicles, the polymer was removed by centrifugation and the treated growth media in the supernatants were used to replace the normal growth medium in the L-asparagine synthetase gene silenced A549 cells. The metabolic activity of the cells was assessed after a proliferation period. 229

Figure 5.25. Metabolic activity over time for gene silenced A549 cells treated with normal medium (black squares), or media exposed to the empty vesicles ($11 \text{ mg} \cdot \text{mL}^{-1}$, cyan diamonds), PEG-ASNS ($0.18 \text{ U} \cdot \text{mL}^{-1}$, red circles), native ASNS ($0.18 \text{ U} \cdot \text{mL}^{-1}$, green diamonds), and ASNS-loaded vesicles ($11 \text{ mg} \cdot \text{mL}^{-1}$ polymer, $0.18 \text{ U} \cdot \text{mL}^{-1}$ protein, purple triangles). The error bars represent the standard deviation from at least 3 repeats. 230

Figure 5.26. Western blot analysis of <i>E. coli</i> cells and GFP elutions from a Nickel-sepharose column. Purified GFP is observed in the RHS lane and non-purified GFP in the center lane. The numbers on the left represent the molar mass in kilodaltons, relative to Precision Plus Protein™ Standards (LHS lane).....	237
Figure 7.1. Turbidimetry curves of polymer 9 at 1 mg·mL ⁻¹ at a programmed heating and cooling rate of 1 °C·min ⁻¹ measured on a Perkin Elmer Lambda 6 instrument (top) and an Agilent Cary 60 instrument (bottom).....	251
Figure 7.2. SEC RI traces for the pNIPAM block copolymers in Chapter 2. mCTA1 (dashed lines in each case) and polymers 1 (A), 2 (B), 3 (C), 4 (D) and 5 (E) are shown. 5 mM NH ₄ BF ₄ in DMF was used as the eluent in each case and the molar mass distributions were calculated against poly(methyl methacrylate) standards.....	252
Figure 7.3. SEC RI traces for the pDEAm block copolymers in Chapter 3. mCTA2 (dashed lines in each case) and polymers 6 (A), 7 (B), 8 (C), 9 (D) and 10 (E) are shown. 2% TEA in THF was used as the eluent in each case and the molar mass distributions were calculated against poly(methyl methacrylate) standards.....	253
Figure 7.4. SEC RI traces for the pDEGMA block copolymers in Chapter 3. mCTA3 (dashed lines in each case) and polymers 11 (A), 12 (B), 13 (C), 14 (D), and 15 (E) are shown. 2% TEA in THF was used as the eluent in each case and the molar mass distributions were calculated against poly(methyl methacrylate) standards.....	254
Figure 7.5. SEC RI traces for the pOEGMA block copolymers in Chapter 3. mCTA4 (dashed lines in each case) and polymers 16 (A) and 17 (B) are shown. 2% TEA in THF was used as the eluent in each case and the molar mass distributions were calculated against poly(methyl methacrylate) standards.....	255

List of Schemes

Scheme 1.1. Outline of the free radical polymerization of styrene to yield poly(styrene) using a thermally activated radical initiator, AIBN, as the radical source.....	6
Scheme 1.2. Generic mechanism for ATRP using a metal-ligand complex (ML) and an alkyl halide initiator. P _n represents the polymer chain. The rate constants in the main equilibrium are shown.....	8
Scheme 1.3. Mechanism for RAFT polymerization using a radical initiator, I-I. The rate constant for each step is shown.....	10
Scheme 1.4. Pre-equilibrium steps during the chain extension of a methacrylate mCTA with an acrylate monomer (A), or the chain extension of an acrylate mCTA with a methacrylate monomer (B).	14
Scheme 1.5. Outline of the photoiniferter mechanism for catalyst- and initiator-free photo-RAFT polymerization. The pre- and main equilibria from conventional RAFT polymerization has been highlighted in green, with additional processes from the iniferter mechanism highlighted in red. Taken from ref. ²⁰	18
Scheme 2.1. Synthesis of pNIPAM-b-[nBA-co-DMA] block copolymers and their subsequent self-assembly in water. Key: x = molar fraction of nBA monomer in the core-forming block.	80

Scheme 3.1. Synthesis of the four corona-forming macroCTA blocks (mCTA1-4) and their subsequent chain extension to yield the amphiphilic diblock copolymers (1-17).	117
Scheme 4.1. Outline of the synthetic and post-synthetic routes employed in this work. Isothermal photoinitiated PISA at 100% light intensity (route A), thermally initiated PISA (route B) and photoinitiated PISA at 20% light intensity (route C) lead to PEG-b-PHPMA nano-objects. Additionally, irradiation of the pre-formed nano-objects formed by either of routes A, B or C, with 100% light intensity (route D), no light (route E) and irradiation at 20% light intensity (route F) leads to a morphological transition in some instances. The morphology diagrams depict the morphologies of PEG ₁₁₃ -b-PHPMA ₃₀₀ at 10 wt%, as an example formulation.	159
Scheme 5.1. Preparation of PEG-b-PHPMA polymersomes with size-selective permeability in a one-pot aqueous photoinitiated RAFT dispersion PISA.....	204

List of Tables

Table 2.1. Block copolymer and resultant particle characterization. Key: ^a determined by ¹ H NMR spectroscopy, ^b determined by SEC (DMF) analysis, ^c R _H of resultant micelles determined by DLS analysis at 20 °C. ^d R _{core} of resultant micelles determined by SLS analysis at 20 °C.....	82
Table 3.1. Properties of the polymers studied in this chapter and in Chapter 2. Key: * M _n calculated from conversion ¹ H NMR spectroscopy. ^a Calculated using ¹ H NMR spectroscopy relative to the polymer end group (mCTA1, 3 and 4) or known mCTA DP (1-17) (see experimental section for details). ^b Calculated from SEC analysis using 2% TEA in THF (mCTA2, mCTA3-4, 6-17) or 5mM NH ₄ BF ₄ in DMF (mCTA1 and 1-5) as the eluent against poly(methyl methacrylate) standards. ^c Calculated from multiple angle DLS analysis using the Stokes Einstein equation. ^d Calculated from multiple angle SLS analysis.	118
Table 3.2. N _{agg} and turbidimetry data for polymers 11-17 . Key: ^a Mean cloud point upon heating the micellar solutions determined using turbidimetry data across from three heating and cooling cycles. ^b For micelles with irreversible transitions, the cloud point from the first heating cycle is shown. ^c The degree of hysteresis from solutions exhibiting irreversible phase transitions was not determined as the normalized transmittance did not reach 0.5 in the cooling cycle. [†] Heated from 10 - 40 °C. [‡] Heated from 50 - 95 °C....	126
Table 4.1. Summary of final conversions as assessed by ¹ H NMR spectroscopy for the 100% light intensity photoinitiated (route A) and thermally initiated (route B) PISA formulations.	161

Acknowledgements

Firstly, I would like to thank my supervisors, Prof. Rachel O'Reilly and Prof. Matthew Gibson, for their mentorship, advice and guidance throughout my time spent at Warwick. I have been very grateful for the scientific freedom they granted me, as well as their eagerness to support me in future endeavors, for which I am extremely appreciative. Thank you both for giving me this opportunity, and for collaborating together on this project. Working with both of you in such a way has been a highlight of my PhD.

I would like to thank all the members of both the O'Reilly and Gibson groups. Having access to your combined expertise and span of scientific research has made my PhD incredibly interesting and engaging. I'm not sure I will ever have a chance to work with such a talented, diverse team of people again and I greatly value this experience. In addition, I would like to thank Dr. Gemma Davies and Prof. Andrew Dove, as well as the members of their research groups. I'd like to also give a special thanks to Mrs. Annie Morton. I would like to acknowledge members both past and present and wish you all the very best for the future.

I would like to thank Dr. Daniel Wright and Dr. Matthew Robin for collaborating with me on my first project and for sharing their knowledge in light scattering analysis and polymer self-assembly, both key components of this thesis. I would like to thank Dr. Helen Willcock and Dr. Craig Bell for all their help at the start of my PhD and for answering every synthetic question I could possibly throw at them. I am also grateful for Dr. Kay Doncom for her advice when starting to work with polymerization-induced self-assembly.

I would like to thank Dr. Saskia Bakker and Dr. Muhammad Hasan for their training and expertise in cryogenic transmission electron microscopy and Western blot analysis, respectively. Dr. Chiara Arno also deserves a massive “thank you!” for all of the cell work and advice on anything bio-related. Additionally, I would like to thank Mr. Rod Wesson for his time in designing and building the photoreactor used to perform all of the light-mediated polymerizations carried out in this Thesis.

Though the work has not been included in this Thesis, I am also grateful for the opportunity to work with all those with which I have had the pleasure of collaborating on projects outside of my own scope. These include Dr. Ignacio Insua and Dr. Francisco Fernandez-Trillo, Miss Emma Brisson, Dr. Daniel Phillips, Dr. Heather Findlay and Prof. Paula Booth, Dr. Elena Lestini, Mr. Robert Keogh, Mr. Spyridon Varlas and Prof. Robert Mathers.

Those of you who have proof-read parts of this thesis: Dr. Rebecca Williams, Miss Maria Inam, Dr. Joseph Jones, Dr. Benoit Couturaud, Mr. Robert Keogh, Mr. Spyridon Varlas, Mr. Jon Husband, Dr. Tom Wilks and Dr. Anne Mabire, you have done an excellent job. All of your advice and discussion has really helped me look at the work from an outsider’s perspective and has undoubtedly improved its contents.

Away from the science, I’d like to thank all of you who have enabled me to work through the times when things didn’t work, helped me accept when papers and grants got rejected, and joined me in celebration when results got published. Those of you at Warwick know who you are. I’d also like to take the opportunity to thank the Tennyson Terriers and all my friends and family back in London for allowing me to escape every now and then, and for reminding me that life exists outside of the Warwick bubble! A special thanks goes to Alex Downes, who convinced me not to quit the course in the first month of my studies.

I'd like to thank my parents, Julia and David Blackman, for their support throughout my undergraduate course at the University of Southampton and my postgraduate studies at the University of Warwick. I'm sure they still have no idea about the contents of this thesis, however they have always listened to my explanations with pride, and for that I am very grateful.

Finally, I would like to thank Charlotte Davison for all the love and patience you have shown me over the past five and a half years. This thesis truly would not have been written without your constant support and kindness. Everywhere I go I'm a tourist but when I'm with you I will always be at home.

Declaration of Authorship

This thesis was composed by myself and has not been submitted previously for the award any degree. The work presented was carried out by myself, except in the following cases:

Chapter 2: Light scattering analysis of micelles comprised of polymers **1** and **4** was performed by Dr. Daniel Wright at the University of Warwick. Rheological analysis was performed with assistance from Miss Laura MacDougall. All differential scanning microcalorimetry experiments were performed by application specialists at Malvern Instruments Ltd. The quantitative ^{13}C NMR spectrum of polymer **5a** and the 500 MHz ^1H NMR spectra of polymers **1** and **4** in deuterium oxide were obtained by Dr. Ivan Prokes at the University of Warwick.

Chapter 3: The synthesis of the RAFT agents 2-Cyano-2-propyl dodecyl trithiocarbonate and 4-cyano-4-(((ethylthio)carbonothioyl)thio) pentanoic acid were performed by Mr. Robert Keogh and Dr. Craig Bell at the University of Warwick, respectively. High resolution electrospray ionization time of flight mass spectrometry was performed by Dr. Lijiang Song at the University of Warwick.

Chapter 4: MALDI-ToF analysis of the PHPMA oligomers was performed by Mr. Jon Husband at the University of Warwick. The synthesis of 4-cyano-4-(((ethylthio)carbonothioyl)thio) pentanoic acid was performed by Dr. Craig Bell, University of Warwick. The design and construction of the photoreactor used for all the light-mediated polymerizations was carried out by Mr. Rod Wesson at the University of Warwick.

Chapter 5: Expression and purification of GFP was carried out by Miss Alice Fayter at the University of Warwick. The *in vitro* assessment of ASNS-loaded vesicles, including the Western blot analysis of the lyzed cell lines, was carried out by Dr. Chiara Arno at

the University of Warwick. Western blot analysis of the enzyme-loaded vesicles was performed with assistance from Dr. Chiara Arno at the University of Warwick. The experimental sections for the *in vitro* studies and the GFP expression and purification were prepared with assistance from Dr. Chiara Arno and Miss Alice Fayter, respectively. Fluorescence microscopy was performed by Dr. Chiara Arno at the University of Warwick. Cryo-TEM analysis was performed with assistance from Mr. Spyridon Varlas and Mr. Robert Keogh at the University of Warwick, except in the case of the salt-free GOx vesicles, whereby the analysis was performed with assistance from Dr. Saskia Bakker at the University of Warwick. The design and construction of the photoreactor used for all the light-mediated polymerizations was carried out by Mr. Rod Wesson at the University of Warwick.

Publications

1. Effect of micellization on the thermoresponsive behavior of polymeric assemblies. L. D. Blackman, D. B. Wright, M. P. Robin, M. I. Gibson and R. K. O'Reilly, *ACS Macro Lett.*, 2015, **4**, 1210-1214.
2. Probing the causes of thermal hysteresis using tunable N_{agg} micelles with linear and brush-like thermoresponsive coronas. L. D. Blackman, M. I. Gibson and R. K. O'Reilly, *Polym. Chem.*, 2017, **8**, 233-244.
3. Comparison of photo- and thermally initiated polymerization-induced self-assembly: a lack of end group fidelity drives the formation of higher order morphologies. L. D. Blackman, K. E. B. Doncom, M. I. Gibson and R. K. O'Reilly, *Polym. Chem.*, 2017, **8**, 2860-2871.
4. Dispersity effects in polymer self-assemblies: a matter of hierarchical control. K. E. B. Doncom, L. D. Blackman, D. B. Wright, M. I. Gibson and R. K. O'Reilly, *Chem. Soc. Rev.*, 2017, **46**, 4119-4134.
5. Permeable protein-loaded polymersome cascade nanoreactors by polymerization-induced self-assembly. L. D. Blackman, S. Varlas, M. C. Arno, A. Fayter, M. I. Gibson, and R. K. O'Reilly, *ACS Macro Lett.*, 2017, **6**, 1263-1267.

Summary of Thesis

This thesis explores the self-assembly and responsive behavior of block copolymer amphiphiles in aqueous solution. In Chapter 1, an overview of the modern synthetic methods used for preparing such materials will be given, as well as the parameters governing block copolymer self-assembly in solution. An introduction into polymerization-induced self-assembly will be given, as well as an overview of stimuli-responsive polymers and polymer self-assemblies. Finally, an outline of the analytical techniques used throughout this thesis for studying polymer self-assemblies will be given.

Chapter 2 will introduce thermoresponsive polymers, which can respond to changes in temperature, before investigating the solution behavior of a series of thermoresponsive polymer self-assemblies. These micelles have a tunable average number of chains per particle and will be used as a platform to investigate the thermoresponsive behavior of the system using a range of complementary solution-based characterization techniques.

Chapter 3 will build on the knowledge gained in the previous chapter and will explore the effects of factors such as the glass transition temperature and hydrogen bonding ability on the thermoresponsive behavior of such systems. This will give an insight into the reversibility of thermoresponsive phase transitions, more generally, and provide a unique tool with which to probe structure-property relationships in stimuli-responsive self-assemblies.

Chapter 4 will uncover the differences between the two initiation pathways for polymerization-induced self-assembly, thermally and photoinitiated, discussed in this Chapter. Isothermal non-equilibrium phase diagrams will be constructed using thermally initiated and photoinitiated polymerization-induced self-assembly. The effects of light intensity on the formed nano-objects will be investigated as well as the effect of post-

synthetic light irradiation, both are aspects that have not been widely explored in the literature.

Chapter 5 will explore the use of polymerization-induced self-assembly to prepare selectively permeable biohybrid vesicular nanoreactors. Functional proteins with fluorescent or enzymatic capabilities will be encapsulated inside hollow polymersomes and the selective permeability of the membrane will be demonstrated. A clinically relevant therapeutic protein will also be investigated as the encapsulated species and the formed nanoreactors' ability to prevent cancer cell proliferation will be validated. The non-covalent, yet protective nature of this protein compartmentalization will also provide several distinct advantages over covalent attachment of poly(ethylene glycol), the current state-of-the-art for this clinical therapeutic.

Finally, Chapter 6 will summarize the conclusions gained from the research herein, as well as offer some insights into possible areas of new research directed by the findings detailed in this thesis.

Abbreviations

[M]	monomer concentration
[M] ₀	initial monomer concentration
\bar{D}	dispersity
α	degree of ionization
α -CT	α -chymotrypsin
β	experimental correction factor in the Siegert relation
δ	chemical shift
η	viscosity
η_0	specific viscosity
η_s	viscosity of the solvent
θ	angle
λ	wavelength
ν	wavenumber
ρ	density
τ	relaxation time
φ	composition
χ	interaction parameter
a_0	area of a surfactant's polar head group
A_2	second virial coefficient
AA	acrylic acid
Abs_x	absorbance at a wavelength of x nm
ACVA	4,4'-azobis(4-cyanopentanoic acid)
A_{fast}	relative amplitude of the fast mode in a light scattering experiment
AM	acrylamide
AN	acrylonitrile
AIBN	2,2'-azobis(2-methylpropionitrile)
AP	alkaline phosphatase
ARGET	activators regenerated by electron transfer
A_{slow}	relative amplitude of the slow mode in a light scattering experiment
ASNS	L-asparaginase
ATRP	atom transfer radical polymerization
AZMB	azomethyl benzoate

B	1,3-butadiene
bCA-II	bovine carbonic anhydrase II
bpy	2,2'-bipyridine
br	broad
BSA	bovine serum albumin
BzMA	benzyl methacrylate
<i>c</i>	concentration
<i>c</i> *	critical entanglement concentration
CAT	catalase
<i>C</i> _{corona}	effective mass concentration of coronal chains
CMC	critical micelle concentration
ConA	Concanavalin A
<i>C</i> _p	heat capacity
cryo-TEM	cryogenic transmission electron microscopy
CTA	chain transfer agent
D	deuterium
<i>D</i>	apparent diffusion coefficient
d	doublet
<i>D</i> ₀	absolute diffusion coefficient
DAAM	diacetone acrylamide
DC	direct current
DCC	<i>N,N'</i> -dicyclohexylcarbodiimide
dd	doublet of doublets
DEAEA	<i>N,N</i> -diethylamino acrylate
DEAm	<i>N,N</i> -diethylacrylamide
DEAMA	<i>N,N</i> -diethylamino methacrylate
DEGMA	diethylene glycol monomethyl ether methacrylate
DEPT	distortionless enhancement by polarization transfer
<i>D</i> _H	hydrodynamic diameter
DLS	dynamic light scattering
DMA	<i>N,N</i> -dimethylacrylamide
DMAEA	<i>N,N</i> -dimethylamino acrylate
DMAEMA	<i>N,N</i> -dimethylamino methacrylate
DMAP	4-(dimethylamino)pyridine
DMB	3,3'-dimethoxybenzidine

DMDMA	(2,2-dimethyl-1,3-dioxolan-4-yl)methyl acrylate
DMF	<i>N,N</i> -dimethylformamide
DMPA	2,2-dimethoxy-2-phenylacetophenone
dn/dc	refractive index increment
DNA	deoxyribonucleic acid
DP	degree of polymerization
dt	doublet of triplets
<i>E. coli</i>	<i>Escherichia coli</i>
ER	endoplasmic reticulum
ESI-MS	electrospray ionization mass spectrometry
ESI-ToF	electrospray ionization time of flight
EY	eosin Y
F	frictional force
FITC	fluorescein isothiocyanate
FT-IR	Fourier transform infra-red
$g_1(q,t)$	electric field autocorrelation function
$g_2(q,t)$	scattering autocorrelation function
GFP	green fluorescent protein
GOx	glucose oxidase
GSH	glutathione
HEA	hydroxyethyl acrylate
HPMA	2-hydroxypropyl methacrylate
HPMAM	2-hydroxypropyl methacrylamide
HRMS	high resolution mass spectrometry
HRP	horseradish peroxidase
I_0	intensity of scattered light at time = 0
ICAR	initiators for continuous activator regeneration
Ig	immunoglobulin
$I_{micelle}$	intensity of dye fluorescence emission at a wavelength corresponding to the sequestered dye
IPTG	isopropyl β -D-1-thiogalactopyranoside
I_{sample}	intensity of scattered light from the sample
$I_{solvent}$	intensity of scattered light from the solvent
$I_{standard}$	intensity of scattered light from the standard

I_{water}	intensity of dye fluorescence emission at a wavelength corresponding to the unsequestered dye in aqueous solution
I_t	intensity of scattered light at time = t
K	contrast factor in SLS analysis
\vec{k}_0	incident wave vector
k_B	Boltzmann constant
k_D	dynamic virial coefficient
\vec{k}_s	scattered wave vector
L	lamellae
LB	lysogeny broth
LAM	less activated monomer
l_c	length of a surfactant's hydrophobic tail
LCST	lower critical solution temperature
LED	light emitting diode
LHS	left hand side
LPO	lactoperoxidase
m	multiplet
m/z	mass to charge ratio
MADIX	macromolecular design <i>via</i> interchange of xanthate
MALDI-ToF MS	matrix-assisted laser desorption/ionization time of flight mass spectrometry
MAM	more activated monomer
mCTA	macromolecular chain transfer agent
MDO	2-methylene-1,3-dioxepane
M_i	mass of chain of length "i"
M_n	number average molar mass
$M_{n, \text{corona}}$	number average molar mass of the corona-forming block
$M_{n, \text{NMR}}$	number average molar mass determined by nuclear magnetic resonance spectroscopy
$M_{n, \text{SEC}}$	number average molar mass determined by size exclusion chromatography
m_{corona}	mass of the corona chains
MLV	multilamellar vesicles
MMA	methyl methacrylate

MRI	magnetic resonance imaging
M_w	weight average molar mass
$M_{w, \text{core}}$	weight average molar mass of the core-forming block
$M_{w, \text{particle}}$	weight average molar mass of the particle
$M_{w, \text{polymer}}$	weight average molar mass of the unimer
n	refractive index
n_0	refractive index of the solvent
N_A	Avogadro's constant
N_{agg}	aggregation number
NaTFA	trifluoroacetic acid sodium salt
n BA	n -butyl acrylate
N_i	number of chains of length "i"
NIPAM	N -isopropylacrylamide
NMP	nitroxide-mediated polymerization
NMR	nuclear magnetic resonance
NVC	N -vinylcarbazole
NVP	N -vinylpyrrolidone
OEGA	oligo(ethylene glycol acrylate)
OEGMA	oligo(ethylene glycol) monomethyl ether methacrylate
OmpF	outer membrane protein F
p	dimensionless packing parameter
P4VP	poly(4-vinyl pyridine)
PAA	poly(acrylic acid)
PAD	poly(N -amidino)dodecylacrylamide)
PAEMA	poly(2-azepane ethyl methacrylate)
PAGMA	poly(o-azidomethyl benzoyl glycerol methacrylate)
PAMAM	poly(amido amine) dendrimer
PAME	poly(L-arginine methyl ester acrylamide)
PAPBA	poly(3-acrylamidophenylboronic acid)
PAZo	poly[6-(4-((4-nitrophenyl)diazenyl)phenoxy)hexyl methacrylate]
PBS	phosphate buffered saline
PBzMA	poly(benzyl methacrylate)
PD	polydispersity
PDAAM	poly(diacetone acrylamide)
PDMS	poly(dimethylsiloxane)

PDEAEA	poly(<i>N,N</i> -diethylamino acrylate)
PDEAm	poly(<i>N,N</i> -diethylacrylamide)
PDEAMA	poly(<i>N,N</i> -diethylamino methacrylate)
PDEGMA	poly(diethylene glycol monomethyl ether methacrylate)
pDMA	poly(<i>N,N</i> -dimethylacrylamide)
PDMAEA	poly(<i>N,N</i> -dimethylamino acrylate)
PDMAEMA	poly(<i>N,N</i> -dimethylamino methacrylate)
PDPMA	poly(2-(diisopropylamino)-ethyl methacrylate)
PEHA	poly(2-ethyl hexyl acrylate)
PEG	poly(ethylene glycol)
PEG-ASNS	L-asparaginase poly(ethylene glycol) conjugate
PEO	poly(ethylene oxide)
PET	photoinduced electron transfer
PGA	poly(glyceryl acrylate)
PGlyMA	poly(glycidyl methacrylate)
PGMA	poly(glyceryl methacrylate)
pH	negative base 10 logarithm of the molar proton concentration
PHPMA	poly(2-hydroxypropyl methacrylate)
PHPMAM	poly(2-hydroxypropyl methacrylamide)
PIAT	poly(3-(isocyano-L-alanyl-aminoethyl)thiophene))
pK_a	negative base 10 logarithm of the acid dissociation constant
pK_{aH}	negative base 10 logarithm of the acid dissociation constant of the conjugate acid
PLMA	poly(lauryl methacrylate)
P_m^\bullet	growing radical chain
PMAA	poly(methacrylic acid)
pMeO _x VAc	poly(oligo(ethylene glycol) vinyl acetate)
PMMA	poly(methyl methacrylate)
PMOXA	poly(2-methyloxazoline)
PMPC	poly(2-(methacryloyloxy)ethyl phosphorylcholine)
P_n^\bullet	growing radical chain
PNA	<i>N</i> -phenyl-1-naphthylamine
<i>pn</i> BA	poly(<i>n</i> -butyl acrylate)
PNBOCA	poly(2-(((2-nitrobenzyl)-oxy)carbonyl)amino)ethyl acrylate)
pNIPAM	poly(<i>N</i> -isopropylacrylamide)

PNBMA	poly(O-nitrobenzyl methacrylate)
POEGA	poly(oligo(ethylene glycol) acrylate)
POEGMA	poly(oligo(ethylene glycol) monomethyl ether methacrylate)
PPMA	poly(pyrenylmethyl methacrylate)
PP-OH	2-hydroxy-4'-2-(hydroxyethoxy)-2-methylpropiophenone
PRE	persistent radical effect
pProlA	poly(<i>N-tert</i> -butoxycarbonyl- <i>O</i> -acryloyl- <i>trans</i> -4-hydroxy-L-proline)
PS	poly(styrene)
PSA	poly(solketal acrylate)
PSPMA	poly[1'-(2-methacryloxyethyl)-3',3'-dimethyl-6-nitrospiro-(2 <i>H</i> -1-benzopyran-2,2'-indoline)]
PISA	polymerization-induced self-assembly
pVDMA	poly(4-vinyl-4,4-dimethylazlactone)
q	quartet
q	scattering wave vector
R	rods
R_θ	Rayleigh ratio of the sample
$R_{\theta, \text{standard}}$	Rayleigh ratio of the standard
RAFT	reversible addition-fragmentation chain transfer
RCA ₁₂₀	<i>Ricinus communis</i> agglutinin
R_{core}	radius of the core
RDRP	reversible deactivation radical polymerization
REPES	regularized positive exponential sum
R_g	radius of gyration
R_H	hydrodynamic radius
RHS	right hand side
RI	differential refractive index
R_{membrane}	vesicle membrane thickness
RNA	ribonucleic acid
ROMP	ring opening metathesis polymerization
RONSS	reactive oxygen, nitrogen and sulfur species
ROP	ring opening polymerization
ROS	reactive oxygen species
S	spherical micelles

s	singlet
SANS	small angle neutron scattering
SAXS	small angle x-ray scattering
SDS	sodium dodecyl sulfate
SEC	size exclusion chromatography
siRNA	small interfering ribonucleic acid
SLS	static light scattering
SOD	superoxide dismutase
SPTP	sodium phenyl-2,4,6-trimethylbenzoylphosphinate
St	styrene
T	absolute temperature
t	triplet
t	time
TEA	triethylamine
T_g	glass transition temperature
T_p	thermal transition temperature determined by differential scanning microcalorimetry
TEM	transmission electron microscopy
TPP	5,10,15,20-tetraphenyl-21H,23H-porphine
UCST	upper critical solution temperature
ULV	unilamellar vesicles
UV	ultraviolet
v	volume of a surfactant's hydrophobic tail
VAc	vinyl acetate
VAZO-44	2,2'-azobis[2-(imidazolin-2-yl)propane] dihydrochloride
V_{core}	volume of the core
V_{corona}	volume of the corona
$V_{\text{lumen total}}$	total volume of the vesicles' lumens
V_H	hydrodynamic volume
V_{internal}	volume of an individual vesicle lumen
V_{membrane}	volume of an individual vesicle membrane
V_{polymer}	volume of an individual polymer chain in the core or membrane
W	worm-like micelles
ZnTPP	5,10,15,20-tetraphenyl-21H,23H-porphine zinc

1.1. Declaration of Authorship

Parts of this Chapter have been published in *Chemical Society Reviews*.

K. E. B. Doncom, L. D. Blackman, D. B. Wright, M. I. Gibson and R. K. O'Reilly,
Chem. Soc. Rev., 2017, **46**, 4119-4134.

6. Conclusions and Outlook

In this thesis, the self-assembly and solution behavior of amphiphilic block copolymer nanoparticles have been studied in aqueous solution. In Chapters 2 and 3, it was found that the N_{agg} of micellar aggregates could be tuned in solution by copolymerization of two monomers with very different aqueous solubility to form the core-forming block, thereby varying the core hydrophobicity of such aggregates. This subtle difference in the solution self-assembly across each series was found to have a marked effect on the reversibility of the thermal phase transition for various LCST-type corona blocks. This was shown to be a result of differences in the core hydration across the series. This micellar platform was then used to investigate the effects of the chemical structure, architecture and physical properties, such as the T_g , on the reversibility of LCST-type transitions, which revealed unprecedented irreversible transitions for coronas with a brush-like architecture.

In addition to the contribution towards the understanding of hysteresis in thermoresponsive polymer systems in this specific example, looking to the future, micelles of such well programmed self-assembly behavior could be used to uncover structure-property relationships for a wealth of other properties. Possible avenues could be their implementation in the study of other stimuli-responsive self-assembled systems, such as those responsive to light, pH, etc. As these assemblies have programmable surface densities, they could also be utilized to study biologically relevant interactions such as those between glycans and lectins, which are known to show a large dependency on shape and multivalency. Other than their potential in uncovering fundamental behavioral relationships, the micelles themselves show potential for biomedical applications. If the responsive corona was functionalized with dyes with a solvochromatic shift, or a hydration-dependent ON/OFF fluorescence output (such as an aminobromomaleimide), the micelles could feasibly be used to monitor an increase in physiological temperatures. A change in physiological temperature is an indicator of a number of diseases and processes, so these micellar assemblies could be used for diagnostic purposes. For

instance, the transition temperature could be tuned such that the micelles were stable at healthy physiological temperatures, but aggregated inside tumors owing to the elevated temperatures typically observed in such an environment. Micelles with brush-like architectures, which showed irreversible transitions, could be designed to aggregate inside the tumor, whilst also switching on the dyes' fluorescence. This would allow for visualization of the tumor as well as potentially limiting the tumor's blood supply through the irreversible aggregation of the particles, which is the basis of embolization therapy.

The self-assembly behavior of various poly(ethylene glycol)-*b*-poly(2-hydroxypropyl methacrylate) (PEG-*b*-PHPMA) nano-objects prepared using aqueous reversible addition fragmentation chain transfer (RAFT) dispersion polymerization-induced self-assembly (PISA) was also studied. Fundamentally, the question was posed of how the self-assembly behavior differed between identical formulations formed by two initiation mechanisms. It was found that those derived from a photoinitiated PISA methodology formed generally higher order self-assembled structures, such as vesicles and lamellae, whereby those formed using thermal initiation had the tendency to form lower order structures, such as spherical and worm-like micelles. The findings from this fundamental study could be used to compare the wealth of literature already published for thermally initiated PISA, to photoinitiated PISA. The former is a self-assembly technique that has gathered considerable attention over the past decade but the latter offers numerous advantages, of which a rapidly growing number of research possibilities are being realized. The effects of altering the experimental parameters, such as the light intensity and the degree of post-synthetic irradiation, were also uncovered, which could be important for certain industrial aspects, such as the scale-up and pilot plant design for preparing such materials. Only once these factors have been considered in detail will PISA-derived self-assembled formulations be able to be translated into numerous potential real life applications (e.g. as rheology modifiers, drug delivery vehicles, gels for cell storage and manipulation, etc.).

Finally, photoinitiated aqueous RAFT dispersion PISA was shown to be a versatile mild synthetic technique for the preparation of PEG-*b*-PHPMA vesicles loaded with functional proteins. These hybrid materials showed fluorescence, catalytic and therapeutic capabilities depending on their encapsulated species. It was shown that the hydrated PHPMA membrane of such vesicles was highly permeable towards small molecules but could act as a robust physical barrier against larger macromolecules such as proteases. This intrinsic property afforded the encapsulated proteins excellent proteolytic stability, even superior to direct PEGylation of L-asparaginase, the current stabilization strategy employed for this clinical biologic. Furthermore, owing to the molecular sieving effect of this membrane, the therapeutic efficacy of this encapsulated species was also demonstrated *in vitro*. As no functionalization of the protein was required, this approach could be applied to a range of therapeutic enzymes in order to improve their pharmacokinetics, which could be explored for the treatment of a wealth of other diseases.

Although the PEG-*b*-PHPMA block copolymer components have been shown in the literature to have good biocompatibility, in order to capitalize on these promising results, the next stage of the research would be to optimize the hydrodynamic volume of these therapeutic vesicles. It is unknown whether these vesicles would show good overall pharmacokinetics, such as favorable clearance pathways etc., owing to their large average diameter of around 350 nm. Smaller vesicles could be achieved by reducing the overall molar mass of the block copolymer, whilst keeping the block ratios the same, or by post-synthetic procedures such as extrusion. Larger vesicles could be investigated for therapeutic applications targeting the stomach or gastrointestinal tract, where large particle sizes become less of an issue. The next steps in investigating the particles' therapeutic potential would be to assess the RAFT agent biocompatibility and the vesicles' *in vivo* biodistribution, clearance mechanism and blood half-life. Additionally, if other therapeutic proteins were encapsulated, which relied on endocytosis for their

therapeutic effect, it would be interesting to explore factors governing endocytosis. These could include investigation into the effect of cross-linking of the vesicles on tissue or tumor penetration or coronal decoration with ligands for active targeting. Additionally, imparting biodegradability into the structure for controlled release or pre-programmable blood half-lives would be a further step in uncovering their therapeutic potential.

It was also shown that the vesicles, separately loaded with distinct enzymes, could interact with one another by way of a cascade. In some regards, this behavior could be considered rudimentary protocell communication. In order to further increase the complexity in such a biomimetic system, it would be of great fundamental interest to enable some sensing capability. This could be in the form of introducing membrane proteins such as porins or transporters, which could selectively allow small molecules to enter the lumen. If such species were gated by the presence of ions, a change in temperature, or pH, certain reactions could be triggered in a modular fashion by the use of external triggers. Better yet, the product of one cascade could be used to gate a reaction between other loaded vesicles present in solution. This behavior would be analogous to the interactions between organelles inside a cell, for instance. However, if membrane proteins were to be incorporated in such a way, the membrane would need to be functionalized or redesigned in order to limit the non-specific permeability of small molecules.

Multi-compartmentalization is another avenue yet to be fully explored in PISA, which could be further utilized to mimic natural cells in terms of their structure. Furthermore, enzyme-loaded vesicles could be designed to synthesize their own functionality, for example biosynthesis of their own functional proteins inside the lumen using external energy and nutrients. The vesicles could also be designed to synthesize amphiphiles inside the lumen, thereby resulting in self-replicating vesicles, another prerequisite for life. Such artificial systems would much better resemble those found in nature.

7. Appendix

7.1. Technical note

It should be noted that the measurement of hysteresis in thermoresponsive polymers in solution is highly dependent on the experimental parameters. It is therefore of utmost importance to use an identical heating and cooling rate when comparing samples. Additionally, the method by which the instrument measures the reference temperature is crucial to the absolute hysteresis value measured. Instruments that use an internal reference cell to measure a volume of water being subjected to identical conditions as the sample (such as a Perkin Elmer Lambda 6 UV/Vis instrument) report more accurate hysteresis values. This is because of the accuracy of the estimation of the true sample temperature upon heating and cooling the sample, which allows the instrument to accurately report the transmittance at the correct temperature, and to maintain an accurate rate of heating and cooling. Instruments that measure the temperature of the coolant water or the heating block during the measurement (such as an Agilent Cary 60 UV/Vis instrument) give somewhat comparable cloud point values upon heating the sample but greatly overestimate the degree of hysteresis owing to errors in estimating the cooling rate of the sample. This can be seen in Figure 7.1, which shows turbidimetry curves for polymer **9** from Chapter 3 measured on both instruments. This issue therefore contributes to discrepancies found throughout the literature in the reported hysteresis values of thermoresponsive polymers, even under seemingly identical conditions, and should be kept in mind when discussing absolute literature hysteresis values. All samples discussed in Chapters 2 and 3 were analyzed on a Perkin Elmer Lambda 6 UV/Vis instrument at a heating and cooling rate of $1\text{ }^{\circ}\text{C}\cdot\text{min}^{-1}$.

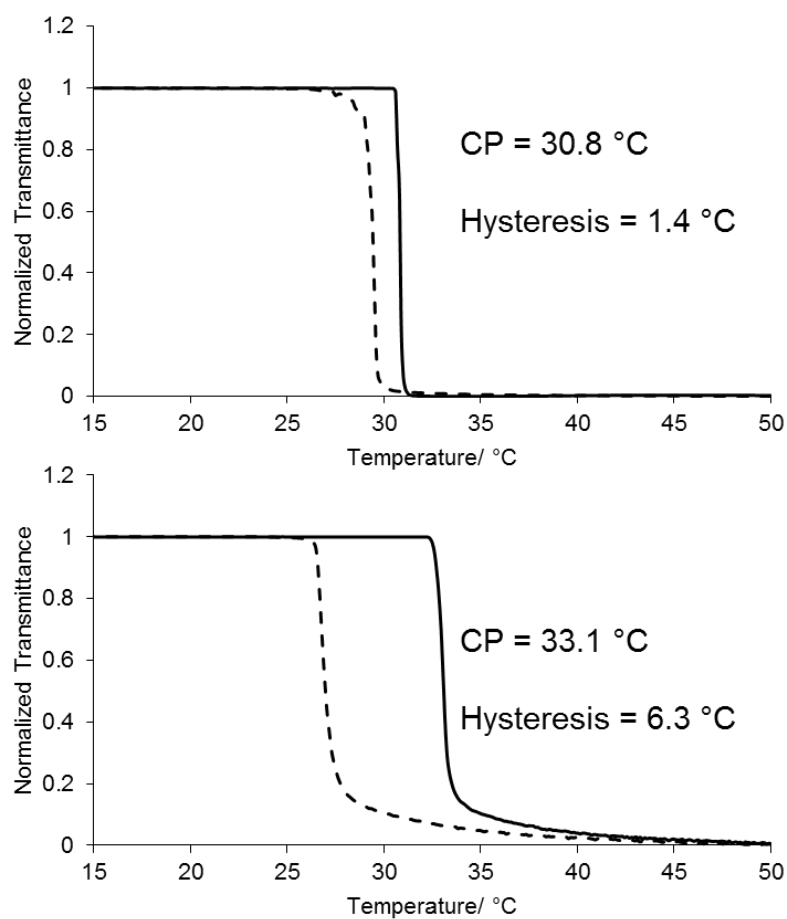


Figure 7.1. Turbidimetry curves of polymer **9** at 1 mg·mL⁻¹ at a programmed heating and cooling rate of 1 °C·min⁻¹ measured on a Perkin Elmer Lambda 6 instrument (top) and an Agilent Cary 60 instrument (bottom).

7.2. Supplementary SEC Data

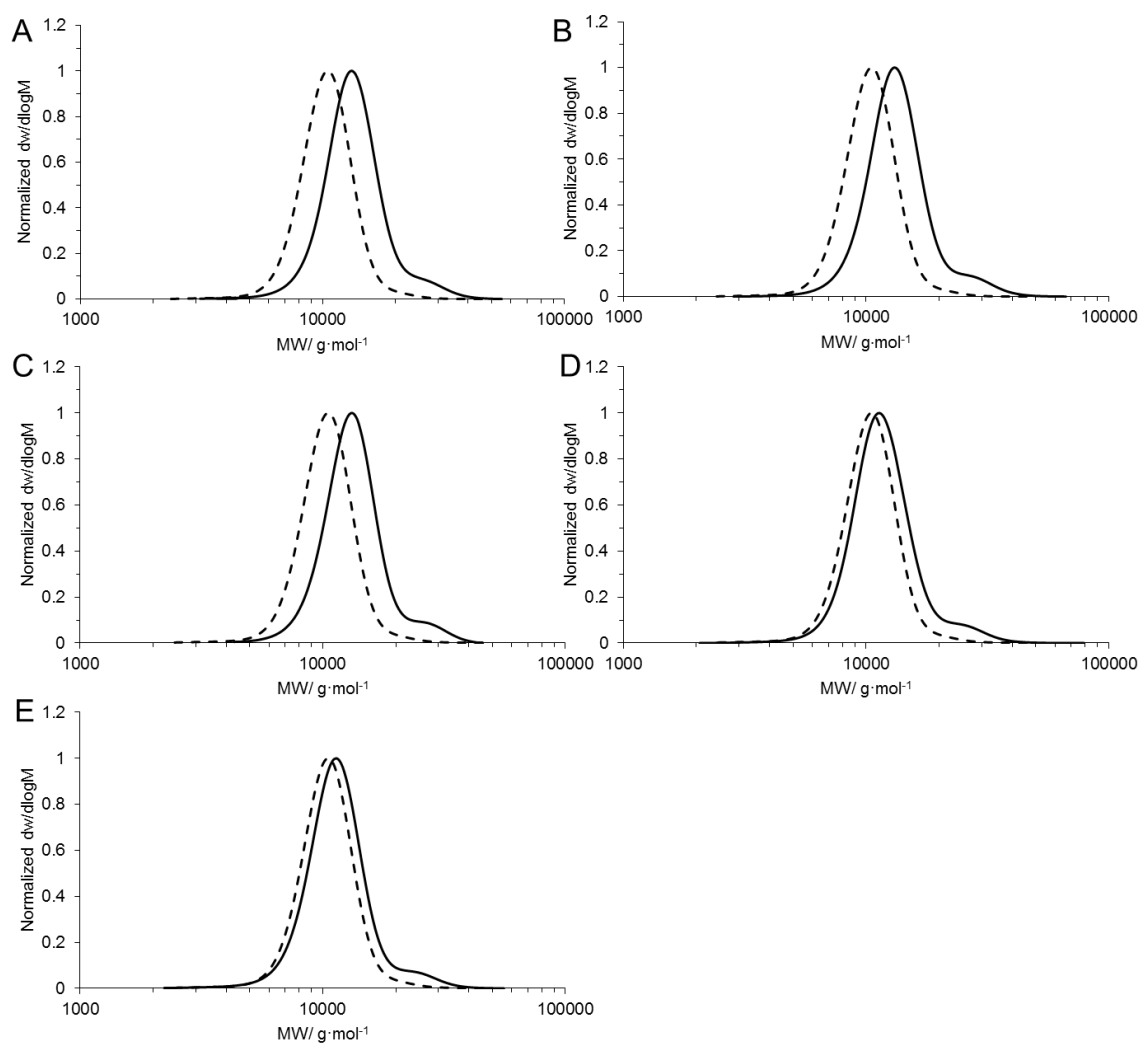


Figure 7.2. SEC RI traces for the pNIPAM block copolymers in Chapter 2. **mCTA1** (dashed lines in each case) and polymers **1** (A), **2** (B), **3** (C), **4** (D) and **5** (E) are shown. 5 mM NH_4BF_4 in DMF was used as the eluent in each case and the molar mass distributions were calculated against poly(methyl methacrylate) standards.

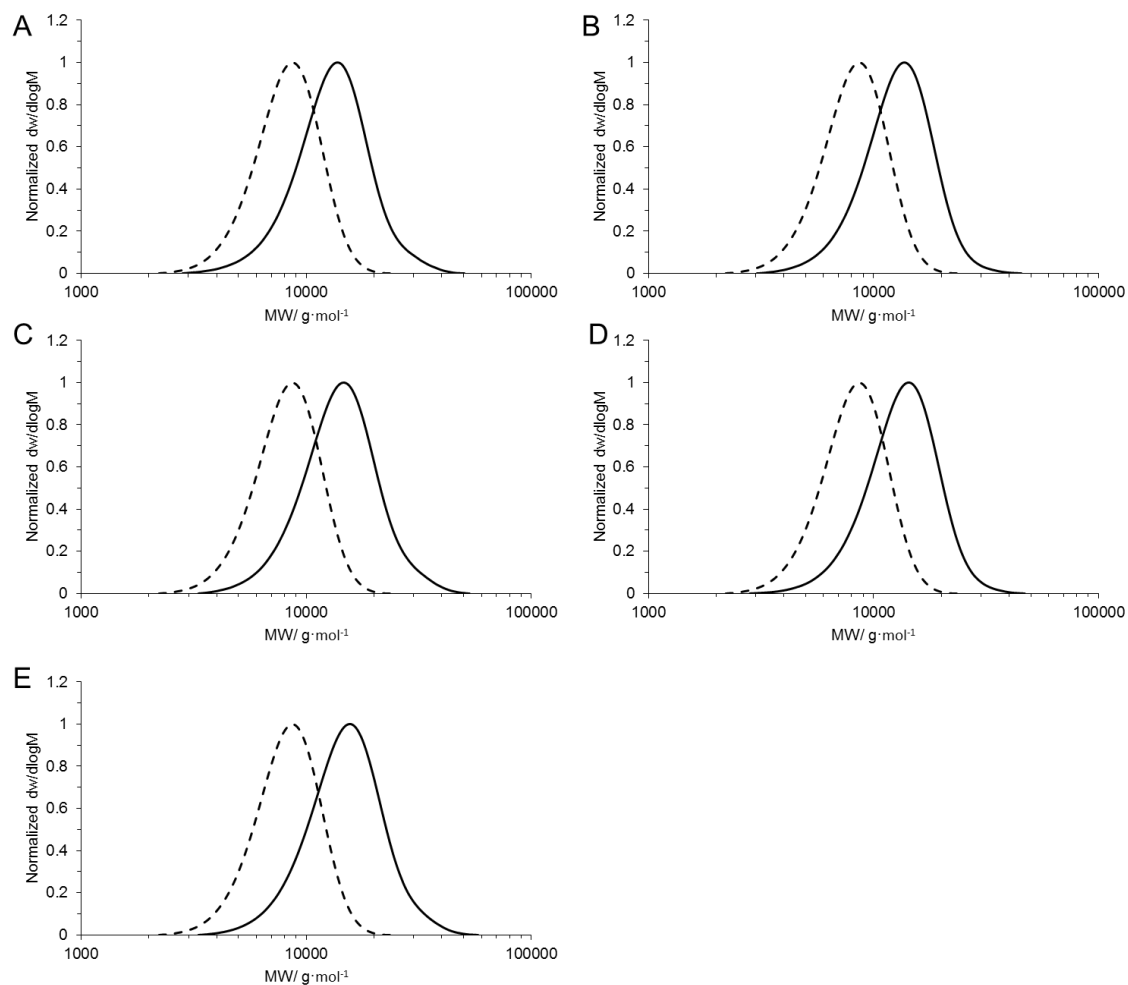


Figure 7.3. SEC RI traces for the pDEAm block copolymers in Chapter 3. **mCTA2** (dashed lines in each case) and polymers **6** (A), **7** (B), **8** (C), **9** (D) and **10** (E) are shown. 2% TEA in THF was used as the eluent in each case and the molar mass distributions were calculated against poly(methyl methacrylate) standards.

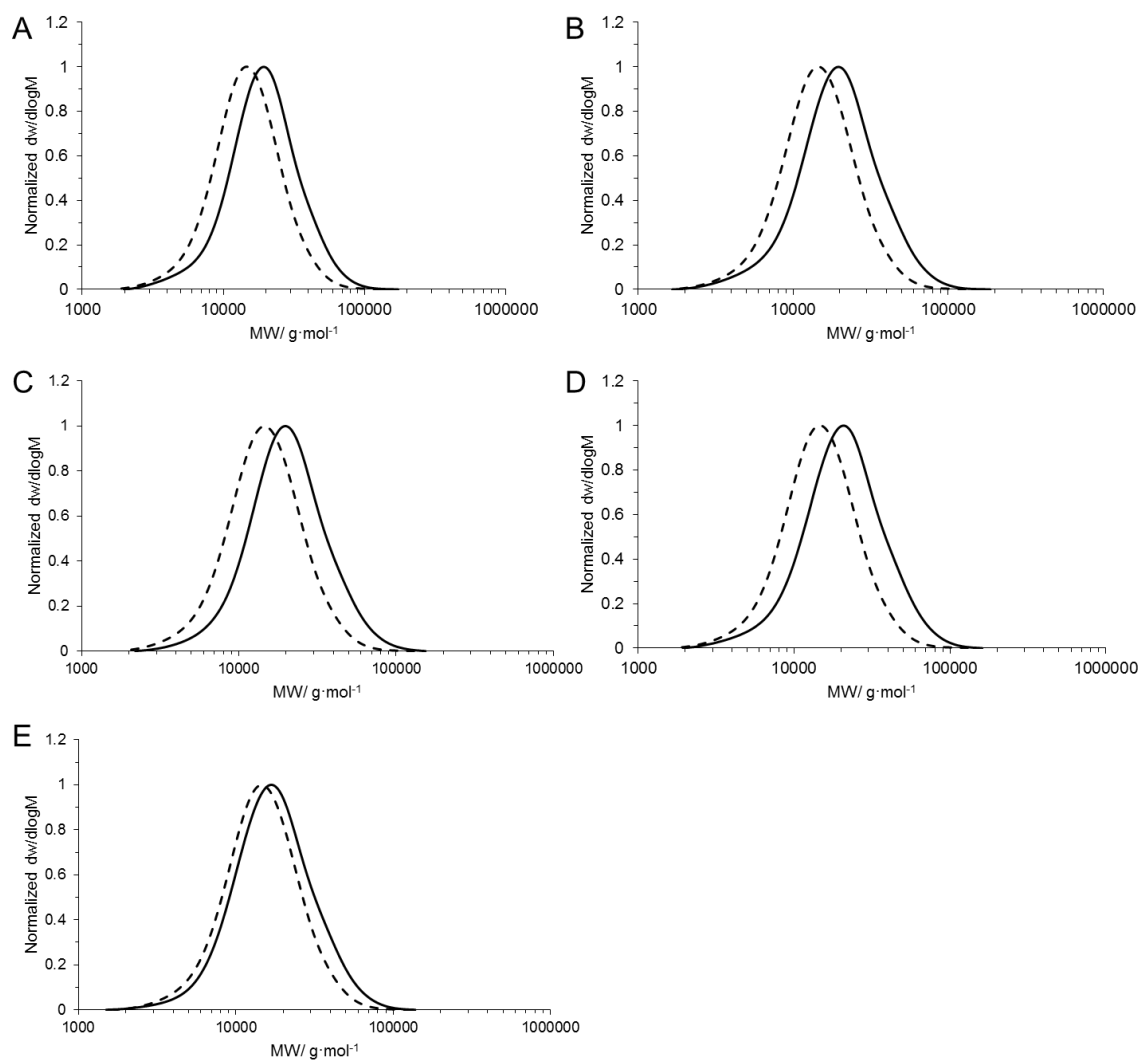


Figure 7.4. SEC RI traces for the pDEGMA block copolymers in Chapter 3. **mCTA3** (dashed lines in each case) and polymers **11** (A), **12** (B), **13** (C), **14** (D), and **15** (E) are shown. 2% TEA in THF was used as the eluent in each case and the molar mass distributions were calculated against poly(methyl methacrylate) standards.

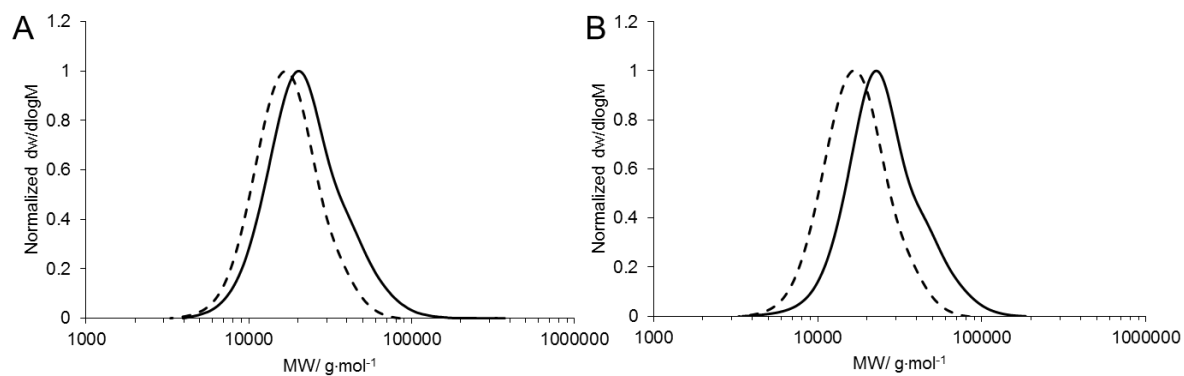


Figure 7.5. SEC RI traces for the pOEGMA block copolymers in Chapter 3. **mCTA4** (dashed lines in each case) and polymers **16** (A) and **17** (B) are shown. 2% TEA in THF was used as the eluent in each case and the molar mass distributions were calculated against poly(methyl methacrylate) standards.